High Efficiency Colloidal Quantum Dot Photovoltaics via Robust Self-Assembled Monolayers

ARTICLE *in* NANO LETTERS · OCTOBER 2015

Impact Factor: 13.59 · DOI: 10.1021/acs.nanolett.5b04797

NANO LETTERS

Letter

pubs.acs.org/NanoLett

High-Efficiency Colloidal Quantum Dot Photovoltaics via Robust Self-Assembled Monolayers

Gi-Hwan Kim,[†,‡] F. Pelayo García de Arquer,[†] Yung Jin Yoon,[‡] Xinzheng Lan,[†] Mengxia Liu,[†] Oleksandr Voznyy,[†] Zhenyu Yang,[†] Fengjia Fan,[†] Alexander H. Ip,[†] Pongsakorn Kanjanaboos,[†,#] Sjoerd Hoogland,[†] Jin Young Kim,[*,‡] and Edward H. Sargent[*,†]

[†]Department of Electrical and Computer Engineering, University of Toronto, 10 King's College Road, Toronto, Ontario M5S 3G4, Canada

[‡]School of Energy and Chemical Engineering, Ulsan National Institute of Science and Technology (UNIST), Ulsan 689-798, South Korea

Supporting Information

ABSTRACT: The optoelectronic tunability offered by colloidal quantum dots (CQDs) is attractive for photovoltaic applications but demands proper band alignment at electrodes for efficient charge extraction at minimal cost to voltage. With this goal in mind, self-assembled monolayers (SAMs) can be used to modify interface energy levels locally. However, to be effective SAMs must be made robust to treatment using the various solvents and ligands required for to fabricate high quality CQD solids. We report robust self-assembled monolayers (R-SAMs) that enable us to increase the efficiency of CQD photovoltaics. Only by developing a process for secure anchoring of aromatic SAMs, aided by deposition of the SAMs in a water-free deposition environment, were we able to provide an interface modification that was robust against the ensuing chemical treatments needed in the fabrication of CQD solids. The energy alignment at the rectifying interface was tailored by tuning the R-SAM for optimal alignment relative to the CQD quantum-confined electron energy levels. This resulted in a CQD PV record power conversion efficiency (PCE) of 10.7% with enhanced reproducibility relative to controls.

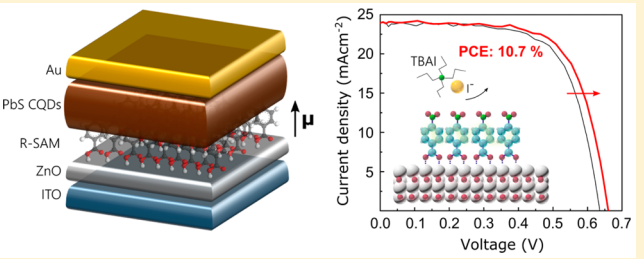

KEYWORDS: *Quantum dot solar cells, high performance, R-SAM, robust, interface, dipole moment*

Colloidal quantum dot (CQD) materials are prominent candidates for optoelectronic and photovoltaic applications in view of their tunable bandgap, ease of processing, low cost, stability and large-area deployability.[1−6] Of particular interest are lead chalcogenide nanocrystals (e.g., PbS and PbSe) whose bandgap can be tailored across the wide solar spectrum.[7,8] The performance of CQD photovoltaic devices has seen progress since their advent and, driven by the advances in the materials science of the CQD solid[9] and the engineering of improved devices,[10,11] certified power conversion efficiencies (PCE) approaching 10% have recently been reported.[12,13]

Now that short-circuit current densities as high as 30 mA/cm^2 have been recently demonstrated,[14] a leading opportunity for further progress lies in improving the open circuit voltage (V_{OC}), which today shows a considerable deficit compared, for example, to the impressively low (E_g−qV_{OC}) of perovskites solar cells.[15] To exploit the bandgap tunability endowed by quantum confinement, it is important to achieve proper band alignment at the interface with the different electron/hole blocking layers, which is a challenging requirement given the finite choice of high-performance metal-oxide electrodes.

Self-assembled monolayers (SAMs) have been extensively used in dye-sensitized and organic solar cells to tailor the energy levels at different material interfaces.[16,17] This is enabled by the electrostatic potential established by the molecule's dipole that results in an effective shift of the local vacuum level. If properly engineered, this can be used to tailor the photovoltaic figures of merit in devices.

To introduce SAMs to produce highly efficient CQD solar cells represents a significant challenge because the sequential use of different solvents and chemically active ligands such as thiols and halides is required for CQD film processing subsequent to SAM application[12] and this is prone to result in SAM damage.[18,19] Successful interface engineering thus requires the SAM be resistant to the chemical reagents used during film formation, be homogeneous, and be highly reproducible.

In this work, we explore for the first time the joint engineering of SAM-tailored interfaces and CQD bandgap, ultimately producing photovoltaic devices with a new record PCE of 10.7%. This is achieved by the manipulation of the interface between CQD active layer and the electron transport

Received: September 11, 2015
Revised: October 22, 2015

DOI: 10.1021/acs.nanolett.5b03677
Nano Lett. XXXX, XXX, XXX−XXX

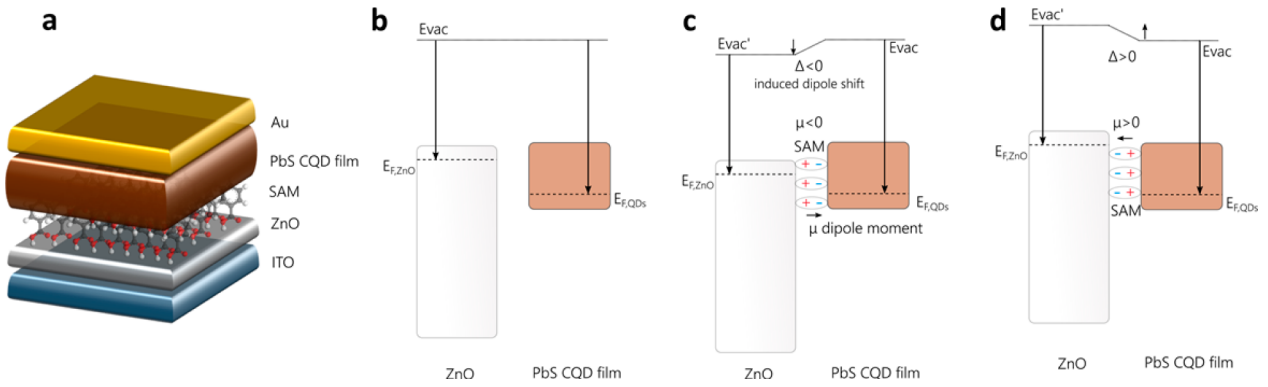

Figure 1. Band-matching for CQD photovoltaics. (a) Representation of a prototypical colloidal quantum dot (CQD) solar cell structure including a SAM between the ZnO and the PbS CQD film. Schematic energy levels of (b) pristine ZnO–PbS junction and SAM-modified interfaces with (c) positive or (d) negative dipole moment molecules. The induced shift on the vacuum level (Δ) depends on the density, dipole, and orientation of the SAM constituent molecules.

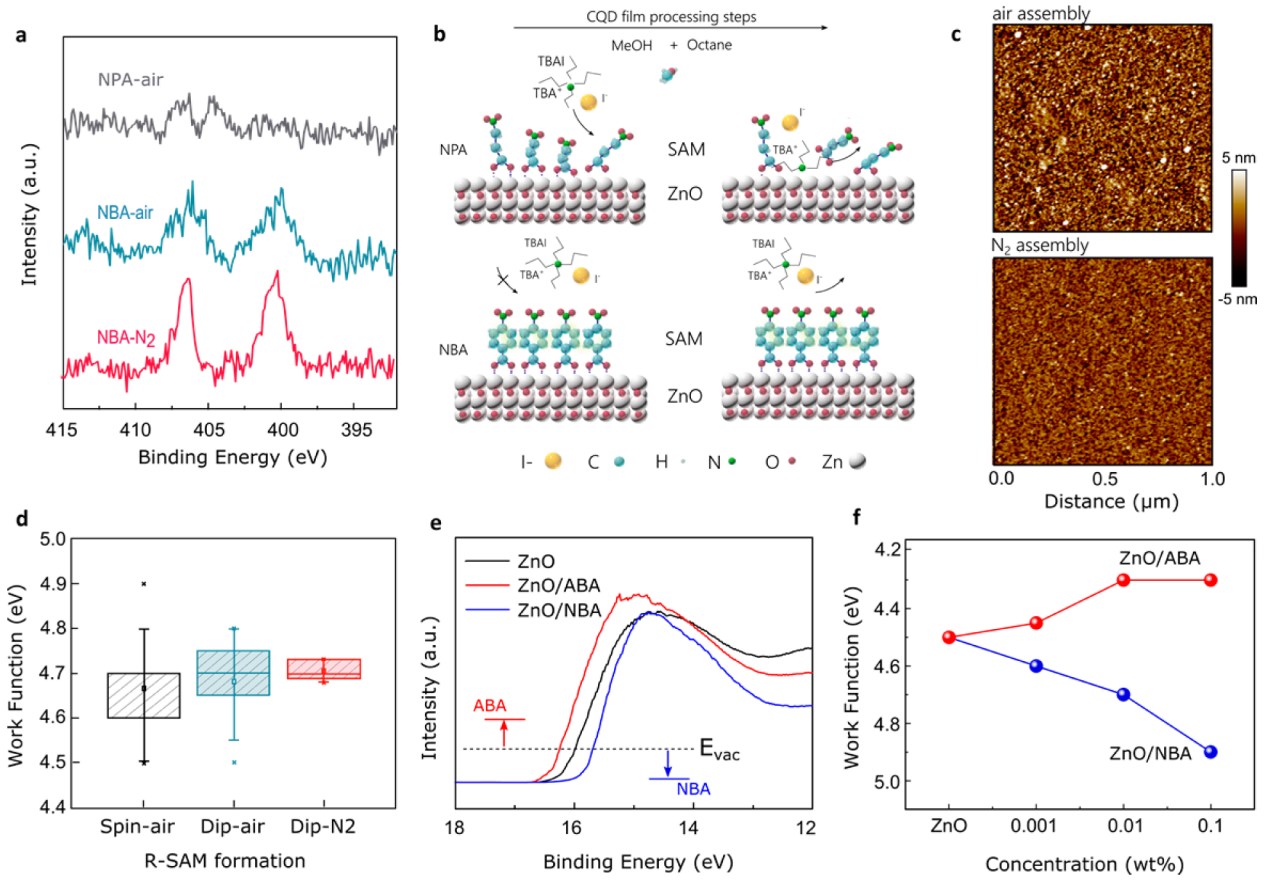

Figure 2. Robust R-SAMs for CQD photovoltaics. (a) XPS spectra of N 1s species of NPA and NBA acids SAMs on ZnO after one CQD ligand exchange step (TBAI + MeOH) shows how aliphatic SAMs are damaged through the process as opposed to conjugated, robust R-SAMs. (b) Schematic illustration of the ligand exchange process. (c) Atomic force micrographs of NBA-modified ZnO substrates in air (top) and N_2 (bottom) assembly conditions. (d) Work function of NBA (0.01%) modified ZnO substrates for different treatment conditions as acquired with Kelvin-probe force measurements. (e) UPS spectra of ZnO (black line), ABA-ZnO (red line), and NBA-ZnO (blue line) at 0.01% concentration plotted relative to an Au reference, illustrating the different trend in the vacuum level shift for different dipole directions. (f) ZnO R-SAM work function variation for different molecule concentrations.

layer using a suite of benzoic-acid-functionalized SAMs that we have developed with the goal of uncompromised quality during ensuing device fabrication. Only by developing a process for secure anchoring of aromatic SAMs, aided by the use of a water-free deposition environment, we were able to provide an interface modification that was robust against ensuing chemical treatments needed in the fabrication of CQD solids. The increased PCE is a result of the improved V_{OC}, a record for a high-performing CQD PV cell at 0.66 V, due to the dipole moment imparted by the monolayer.[17]

The structure of the CQD photovoltaic devices is shown in Figure 1a. Briefly (for detailed fabrication see Experimental Section), a ZnO layer is deposited by spin-casting on top of an indium tin oxide (ITO) electrode. These electrodes are then

DOI: 10.1021/acs.nanolett.5b03677
Nano Lett. XXXX, XXX, XXX–XXX

functionalized using various SAMs, each of which employs a carboxylic acid binding group known to attach to metal oxide semiconductors such as ZnO.[20,21] The photoactive CQD film is subsequently deposited in layer-by-layer fashion. The originally oleic-acid capped CQDs are subject to a solution-phase iodine treatment and then fully exchanged during film formation using tetrabutylammoniun iodide (TBAI) as previously reported.[10−12] An electron blocking layer consisting of 2 layers of 1,2-ethanedithiol (EDT) exchanged CQDs is spin-cast prior to application of a gold electrode contact.[11]

It is known that the molecular dipole (μ_{mol}) can be adjusted in magnitude and direction by judiciously varying the functionality at the opposite site of the carboxylic group.[17] In this a way, the energy levels of the ZnO substrate can be tailored (Figure 1b). For example, molecules exhibiting a positive dipole moment are expected to produce a downward shift of the vacuum level at the interface (Figure 1c). In contrast, negative dipole moment molecules will push the ZnO energy levels upward (Figure 1d). The effective net energy shift (Δ) is a function of the SAM density (N) and orientation (θ) in such a way interfacial energy levels can be finely controlled[17,18]

$$\Delta = \frac{Nq\mu_{mol}\cos(\theta)}{\varepsilon_0\varepsilon_r} \quad (1)$$

Here q, ε_0, and ε_r are respectively the elementary charge, vacuum, and relative permittivity of the molecules. If properly mastered, SAMs can be used to match the optimum energy levels at the ZnO interface, leading to maximized open-circuit voltage.

To evaluate the conditions for chemically stable SAMs during CQD device fabrication, we functionalized ZnO substrates using a suite of different SAMs and subjected them to the relevant ensuing CQD-processing chemical steps. SAMs were built by immersing the as-deposited ZnO substrates into solutions of the different molecules (see Experimental Section for details on SAM fabrication). 3-Nitropropionic acid (NPA) and 4-nitrobenzoic acid (NBA) were chosen in view of their similar functional characteristics (carboxylic and nitro groups) and dipole moments but different morphologies (aliphatic versus aromatic character). The presence of the SAMs after incubation was first assessed using X-ray photoemission spectroscopy (XPS) measurements (Supporting Information Figure S1 and S2). We then subjected the functionalized ZnO substrates to CQD solid film fabrication conditions: a sequential combination of ligands (tetrabutylammonium iodide, TBAI) and orthogonal solvents (methanol and octane).[11,12] We were concerned that these treatments could potentially lead to SAM degradation by the halogenation of its constituent molecules, the modification of their anchoring mode, or the substitution of coordinated ZnO−COOH bonds.[22,23]

We found that, after we exposed the SAMs to TBAI and methanol, NPA SAMs were indeed damaged, as revealed by XPS measurements (Figure 2a). In contrast, NBA SAMs remain present following the same fabrication conditions, as no modification in either XPS peak position or intensity was evident. This suggests that the structure of the SAM molecules plays a significant role in determining the robustness of SAMs during ensuing CQD film processing. We propose that this may arise from the strong $\pi-\pi$ interaction taking place between the conjugated benzene rings that ultimately leads to a more ordered and uniformly oriented SAM sterically protected against attacking reagents (Figure 2b). In contrast, aliphatic SAMs exhibit more degrees of freedom resulting in less ordered SAMs and the exposure of a higher number of reactive sites. This could result in damage to the SAM because aliphatic molecules are more prone to iodide halogenation compared to the aromatic molecules.[24,25]

These studies led us to select aromatic molecules as the candidate family for robust SAMs compatible with high-efficiency CQD photovoltaics.

In order to ensure the compactness and reproducibility of the SAM substrate modification, a crucial aspect that needs to be assessed for photovoltaic applications, we then investigated different assembly conditions. During the formation of the SAM, several competing processes, such as the adsorption of water or oxygen species, can undermine self-assembly, resulting in molecule clustering and incomplete SAM morphologies.[26] These would fail to provide the spatially uniform and reliable increase desired in solar cell performance. The problem is evidenced in Figure 2c in which atomic force microscopy reveals the presence of molecule aggregates in the case of substrates incubated under ambient environmental conditions.

In striking contrast, inert incubation leads to uniform, pinhole-free, SAMs. Kelvin probe microscopy reveals that the air-processed SAMs showed uncontrolled work functions, while SAMs applied in an inert environment showed a much narrower distribution of electronic properties (Figure 2d).

In sum, only by combining aromatic SAMs and inert processing conditions (robust self-assembled monolayer (R-SAM)) were we able to obtain reproducible SAMs that were robust against CQD film processing.

In order to modify the energy level of the ZnO in a controlled way, different moieties were incorporated to the benzene ring to modify its associated dipole moment ($-NO_2$, NBA, + 3.8D and $-NH_2$, 4-aminobenzoic acid (ABA), −4.5D). The different vacuum level shift at the ZnO surface after R-SAM treatment was assessed using ultraviolet photoelectron spectroscopy (UPS). Figure 2e reveals the modification in the vacuum level following R-SAM formation. A consistent trend is observed correlating with the opposite sign of NBA and ABA molecule dipoles (see inset).

The concentration of the R-SAM and the associated energy shift was controlled using different concentrations during the incubation procedure (see Experimental Section). Contact angle measurements were carried out to corroborate the different monolayer coverage at various ABA or NBA concentrations (Supporting Information Figure S3). The increase in the contact angle observed under heavier treatments indicates a greater hydrophobicity of the ZnO substrates, consistent with increased R-SAM coverage.[17,27]

Figure 2f shows the work function of the functionalized substrates for various NBA/ABA concentrations compared to that of the bare ZnO substrate as measured by Kelvin-probe force microscopy. Following ABA treatment, the work function decreases by up to 0.2 eV. In contrast, the work function of NBA functionalized substrates is pushed down by 0.4 eV for the highest of the NBA concentrations. This trend is in good agreement with the expected behavior revealed by UPS (see Supporting Information Figure S4).

To evaluate the impact that the R-SAM dipole could have on solar cell performance, we built an optoelectronic model that takes into account relevant material parameters such as solar light absorption, energy levels, transport, and density of states (see Supporting Information Table S1 for modeling details). By

DOI: 10.1021/acs.nanolett.5b03677
Nano Lett. XXXX, XXX, XXX−XXX

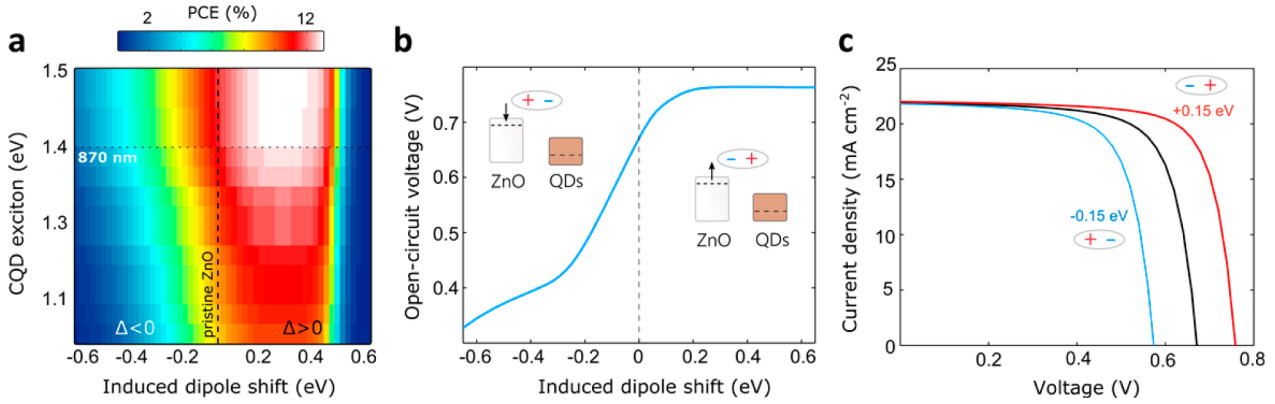

Figure 3. Jointly tuning CQD exciton energy and induced dipole shift toward maximized photovoltaic performance. (a) In the absence of a dipole shift, maximum PCEs are predicted for CQDs with exciton energies in the 1.4−1.5 eV range. Further improvements are only within reach by introducing a positive dipole shift. (b) Variation of open-circuit voltage as a function induced shift for 1.4 eV CQDs (dashed-horizontal line of panel a). (c) Simulated current−voltage characteristics under AM1.5G illumination for induced dipole shifts of −0.15, 0, and +0.15 eV. The complete set of photovoltaic figures of merit is shown in Supporting Information Figure S5.

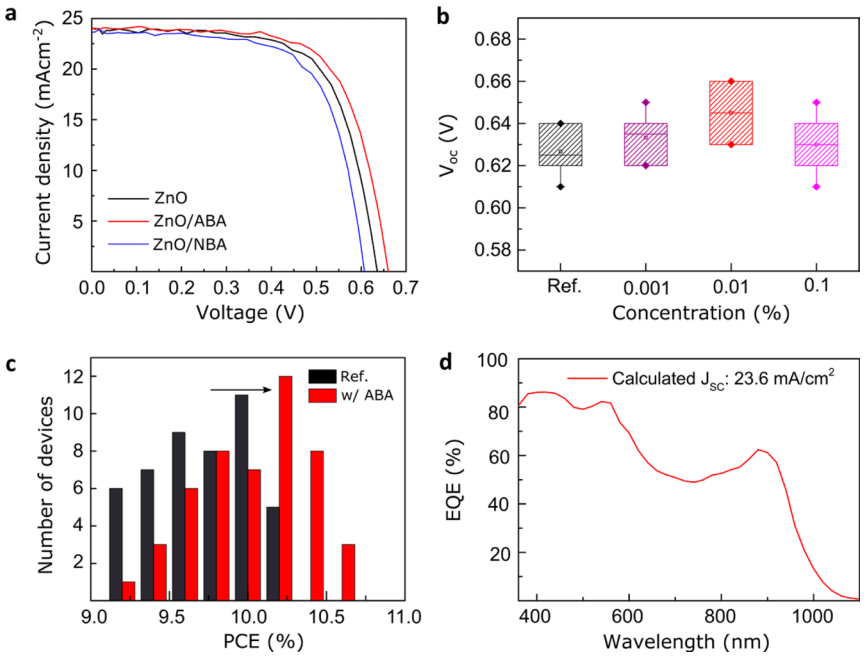

Figure 4. Optimizing device performance via R-SAM modification. (a) Current−voltage characteristics of CQD 1.4 eV devices with ABA and NBA R-SAMs. (b) Open-circuit voltage for various concentration of ABA layer. (c) PCE histogram of the devices with or without ABA layer (0.01% concentration). (d) External quantum efficiency of a representative ABA 0.01% device.

doing so, we could determine the relation between CQD exciton energy and ZnO electron affinity in the overall optimization of PCE. In Figure 3a, we plot the calculated PCE as a function of CQD exciton energy and induced dipole shift. In the absence of a dipole layer, the simulated PCE peaks for a CQD exciton peak at 1.3−1.5 eV. Encouragingly, under these conditions electrostatic modification of the ZnO/CQD PbS interface could result in a further improvement of 1 PCE point if molecules with a positive dipole are used. This comes as a consequence of the associated improvement in the open-circuit voltage (Figure 3b), which increases from a baseline value of 0.66 V under the presence of a positive dipole shift (increasing the local vacuum energy, e.g., using ABA R-SAMs). A maximum V_{OC} increase of 90 mV is feasible, beyond which further increasing the dipole shift results in a significant reduction of electron injection and short-circuit current and this pins the attainable open-circuit voltage and leads to a decrease in the net PCE (the complete set of photovoltaic figures of merit is shown in Supporting Information Figure S5). Both control and R-SAM modified devices retain their stability and show hysteresis-free behavior when stored in ambient conditions over the course of an initial 30 day study (Supporting Information Figures S6 and S7). The use of molecules with a negative dipole (e.g., NBA) is expected to result into a rapid reduction in the open-circuit voltage. The aforementioned scenario is illustrated in Figure 3c, where the V_{OC} variation under the presence of different induced dipole shifts is depicted.

We then sought to take advantage of vacuum level modulation offered by the R-SAM. We fabricated photovoltaic devices based on ZnO dipole-engineered substrates and CQDs exhibiting an excitonic peak at 1.41 eV. Current density versus

DOI: 10.1021/acs.nanolett.5b03677
Nano Lett. XXXX, XXX, XXX−XXX

voltage characteristics under 100 mW/cm^2 AM1.5G irradiation of devices prepared on ABA (negative dipole moment), NBA (positive dipole moment), and pristine ZnO substrates are shown in Figure 4a (device performance summarized in Table 1). As hypothesized, the modification of the energy level after ABA treatment (0.01%) gives rise to a notable increase in V_{OC}, and this reaches a new record value of 0.66 V. An improvement in FF is also observed due to reduced back-recombination. As a consequence, the solar PCE is enhanced from 10.2% to 10.7%. This is the highest PCE reported to date for a CQD photovoltaic device. In contrast, when NBA R-SAMs are used both V_{OC} and PCE decrease, a fact attributed to the opposite orientation of their dipole moments. The performance of cells for various concentrations of ABA and NBA is shown in Supporting Information Figure S8 and their figures of merit listed in Supporting Information Table S2 and S3.

Table 1. Device Characteristics of CQD Photovoltaics with and without R-SAMs Layer

structure	J_{SC} (mA cm^{-2})	V_{OC} (V)	FF	PCE (%)
ITO/ZnO/PbS/Au	23.68	0.64	67.89	10.2
ITO/ZnO/ABA/PbS/Au	23.95	0.66	68.06	10.7
ITO/ZnO/NBA/PbS/Au	23.62	0.60	67.18	9.6

To further investigate the effects of ABA interface modification, as well their reproducibility, we characterized the performance of over 50 cells subjected to ABA R-SAM modification. A box-plot of the open-circuit voltage as a function of ABA concentration is shown in Figure 4b. This diagram reveals a consistent improvement over the control case once R-SAMs are used. A histogram of the PCE for both optimized and reference samples is shown in Figure 4c. We report an average PCE of 9.8% (±0.4%) for standard devices and a PCE of 10.2% (±0.4%) for optimized ABA R-SAMs. The external quantum efficiency (EQE) of a representative ABA 0.01% device is shown in Figure 4d, illustrating the high EQE at the exciton peak (up to 60%) and the good agreement between predicted and measured J_{SC}.

On the basis of our predictions (Figure 3a), we then sought to verify that the interface modification using R-SAMs could be exploited for other CQD sizes. We built devices based on smaller-bandgap CQDs (1.3 eV exciton energy, Supporting Information Figure S9). An additional 0.75 power point was obtained due to the increase in V_{OC} (plus 20 mV, raising V_{OC} up to 0.6 V) and FF (+0.02). This showcases the opportunity for R-SAMs to extend further PV response into the infrared region via band alignment tailoring.[28]

Conclusion. This work constitutes the first report in which interface-modifying SAMs led to enhanced CQD PV performance. R-SAMs take advantage of the strong $\pi-\pi$ interaction of benzene rings, enabling them to withstand the otherwise damaging effects of CQD film ligand exchange processing. The secure anchoring of aromatic R-SAMs, aided by the use of assembly in an inert environment, resulted in reproducible interface modification that was robust against ensuing chemical treatments needed in the fabrication of CQD solids. By incorporating R-SAMs consisting of amine or nitro functional groups, we tailored band alignment advantageously at the PbS-CQD/ZnO interface. This led to a record PCE of 10.7%, primarily due to improvements in V_{OC} (up to 0.66 V) and FF. We jointly explored R-SAM interface modification and quantum dot tunability, demonstrating that the aforementioned benefits also hold for different CQD bandgaps. This suggests avenues for further improvements such as the incorporation of R-SAMs in tandem CQD architectures that maximize solar energy harvesting.[7,8]

Experimental Section. *CQD Synthesis.* PbS QDs were prepared following previous reports.[5] The nanoparticles were separated from the growth solution by using acetone and then dried in vacuum and redispersed in toluene (150 mg/mL) and transferred to a nitrogen glovebox. Methanol was used to precipitate the nanocrystals then centrifuged to isolate the PbS nanoparticles. This washing step was repeated several times. Following full drying, the nanocrystals were finally dispersed in octane (50 mg/mL). Iodine molecular passivation was following the previous reported.[12]

ZnO Film Deposition. The synthesis of ZnO nanoparticles is similar to previously reported method.[21] After the synthesis of ZnO, the ZnO solution is kept at room temperature for 24 h with vigorous stirring. For the ZnO film, the ZnO solution was spin-cast on ITO glass at 3000 rpm for 30 s then annealing the substrate at 200 °C for 10 min.

R-SAM Fabrication. Robust self-assembled monolayers were fabricated by soaking ZnO substrates into SAM molecules solutions (ABA and NBA were dissolved in anhydrous methanol under a N_2 atmosphere) for 1 min and then rinsed in pure methanol after incubation. Substrates were then annealed at 100 °C for 10 min. The fabrication method was optimized to ensure compatibility with subsequent CQD processing steps, as well as to provide with a good reproducibility (see Supporting Information Figure S10).

Device Fabrication. PbS CQD films were fabricated by a layer-by-layer spin-casting process. PbS CQDs in octane (50 mg/mL) were deposited onto the ZnO substrates and spin-casted at 2500 rpm for 10 s. TBAI (10 mg/mL) in methanol solution was deposited on the PbS CQD film and spun after 30 s at the same speed for 10 s then followed by two rinsing steps with methanol. The process was repeated 8 times. After completion of the PbS-TBAI layer, two layers of ethane dithiol (EDT) exchanged CQDs (0.01 vol % in acetonitrile solution) were deposited. For the top electrode, 120 nm Au was deposited on the PbS CQD film for making complete the device.

Device Characterization. J–V Characterization. The current–voltage characteristics were measured using a Keithley 2400 source-meter in N_2 atmosphere. The solar spectrum at AM1.5 was simulated to within class A specifications (less than 25% spectral mismatch) with a Xe lamp and filters (Solar Light Company Inc.) with measured intensity at 100 mW/cm^2. The source intensity was measured using a Melles–Griot broadband power meter and a Thorlabs broadband power meter through a circular 0.049 cm^2 aperture at the position of the device and confirmed with a calibrated reference solar cell (Newport, Inc.). The accuracy of the power measurement was estimated to be ±5%.

EQE Measurement. External quantum efficiency spectra were taken by subjecting the cells to monochromatic illumination (400 W Xe lamp passing through a monochromator and appropriate cutoff filters). The output power was calibrated with Newport 818-UV and Newport 838-IR photodetectors. The beam was chopped at 220 Hz and focused in the pixel together with a solar-simulator at 1 sun intensity to provide for light bias. The response of the cell was acquired with a Lakeshore preamplifier connected to Stanford Research 830 lock-in amplifier at short-circuit conditions.

DOI: 10.1021/acs.nanolett.5b03677
Nano Lett. XXXX, XXX, XXX–XXX

XPS and UPS Measurement. XPS and UPS measurements were carried out using a ESCALAB 250XI from Thermo Fisher Scientific. He I $h\nu$ = 21.22 eV was used as a light source and thermally evaporated Au substrates were used as a reference for UPS. Workfunctions (Φ) were calculated from the onset of the secondary edge (E_{SE}) using the equation $\Phi = 21.22 - E_{SE}$. Valence band edges were taken relative to an Au reference with known Fermi energy.[29]

Electrical Modeling. CQD photovoltaic devices were modeled with SCAPS[30,31] simulation software. Parameter space and simulation details are available in Supporting Information Table S1.

■ ASSOCIATED CONTENT

Supporting Information

The Supporting Information is available free of charge on the ACS Publications website at DOI: 10.1021/acs.nanolett.5b03677.

A detailed description of XPS, UPS contact angle, $J-V$ characteristics with various concentrations of ABA and NBA on ZnO substrate, as well as additional electrical modeling and histogram of performance with different fabrications. (PDF)

■ AUTHOR INFORMATION

Corresponding Authors

*E-mail: ted.sargent@utoronto.ca (E.H.S.).
*E-mail: jykim@unist.ac.kr (J.Y.K.).

Present Address

#P.K.: Materials Science and Engineering, Faculty of Science, Mahidol University, 272 Rama 6 Rd., Ratchathewi District, Bangkok, 10400, Thailand.

Author Contributions

G.-H.K and F.P.G.d.A contributed equally to this work.

All authors discussed the results and assisted during manuscript preparation.

Notes

The authors declare no competing financial interest.

■ ACKNOWLEDGMENTS

This publication is based in part on work supported by Award KUS-11-009-21, made by King Abdullah University of Science and Technology (KAUST), by the Ontario Research Fund - Research Excellence Program, by the Natural Sciences and Engineering Research Council (NSERC) of Canada, and by the International Cooperation of the Korea Institute of Energy Technology Evaluation and Planning (KETEP) grant funded by the Korea government Ministry of Knowledge Economy (2012T100100740). We thank Emre Yassitepe and Cao-Thang Dinh for helpful discussions. We also thank E. Palmiano, L. Levina, A. Labelle, R. Wolowiec, and D. Kopilovic for their help over the course of this study.

■ REFERENCES

(1) Hines, M. A.; Scholes, G. D. *Adv. Mater.* **2003**, *15*, 1844−1849.
(2) Gur, I.; Fromer, N. A.; Geier, M. L.; Alivisatos, A. P. *Science* **2005**, *310*, 462−465.
(3) Mcdonald, S. A.; Konstantatos, G.; Zhang, S.; Cyr, P. W.; Klem, E. J.; Levina, L.; Sargent, E. H. *Nat. Mater.* **2005**, *4*, 138−142.
(4) Kamat, P. V. *J. Phys. Chem. C* **2008**, *112*, 18737−18753.
(5) Pattantyus-Abraham, A. G.; Kramer, I. J.; Barkhouse, A. R.; Wang, X.; Konstantatos, G.; Debnath, R.; Levina, L.; Raabe, I.; Nazeeruddin, M. K.; Grätzel, M. *ACS Nano* **2010**, *4*, 3374−3380.
(6) Kim, G. H.; Walker, B.; Kim, H. B.; Kim, J. Y.; Sargent, E. H.; Park, J.; Kim, J. Y. *Adv. Mater.* **2014**, *26*, 3321−3327.
(7) Sargent, E. H. *Nat. Photonics* **2012**, *6*, 133−135.
(8) Graetzel, M.; Janssen, R. A.; Mitzi, D. B.; Sargent, E. H. *Nature* **2012**, *488*, 304−312.
(9) Ip, A. H.; Thon, S. M.; Hoogland, S.; Voznyy, O.; Zhitomirsky, D.; Debnath, R.; Levina, L.; Rollny, L. R.; Carey, G. H.; Fischer, A.; et al. *Nat. Nanotechnol.* **2012**, *7*, 577−582.
(10) Ning, Z.; Voznyy, O.; Pan, J.; Hoogland, S.; Adinolfi, V.; Xu, J.; Li, M.; Kirmani, A. R.; Sun, J.-P.; Minor, J.; Kemp, K. W.; Dong, H.; Rollny, L.; Labelle, A.; Carey, G.; Sutherland, B.; Hill, I.; Amassian, A.; Liu, H.; Tang, J.; Bakr, O. M.; Sargent, E. H. *Nat. Mater.* **2014**, *13*, 822−828.
(11) Chuang, C.-H. M.; Brown, P. R.; Bulović, V.; Bawendi, M. G. *Nat. Mater.* **2014**, *13*, 796−801.
(12) Lan, X.; Voznyy, O.; Kiani, A.; García de Arquer, F. Pelayo; Abdullah, S. A.; Kim, G. H.; Liu, M.; Yang, Z.; Walters, G.; Jixian, X.; Yuan, M.; Ning, Z.; Fan, F.; Kanjanaboos, P.; Kramer, i.; Zhitomirsky, D.; Lee, P.; Perelgut, A.; Hoogland, S.; Sargent, E. H. *Adv. Mater.* **2015**, DOI: 10.1002/adma.201503657.
(13) National Center for Photovoltaics. http://www.nrel.gov/ncpv/ (accessed October 16, 2015).
(14) Carey, G. H.; Levina, L.; Comin, R.; Voznyy, O.; Sargent, E. H. *Adv. Mater.* **2015**, *27*, 3325−3330.
(15) Yang, W. S.; Noh, J. H.; Jeon, N. J.; Kim, Y. C.; Ryu, S.; Seo, J.; Seok, S. I. *Science* **2015**, *348*, 1234−1237.
(16) Krüger, J.; Bach, U.; Grätzel, M. *Adv. Mater.* **2000**, *12*, 447−451.
(17) Goh, C.; Scully, S. R.; McGehee, M. D. *J. Appl. Phys.* **2007**, *101*, 114503−114503.
(18) Love, J. C.; Estroff, L. A.; Kriebel, J. K.; Nuzzo, R. G.; Whitesides, G. M. *Chem. Rev.* **2005**, *105*, 1103−1170.
(19) Tekin, N.; Cebe, M.; Tarımcı, Ç. *Chem. Phys.* **2004**, *300*, 239−246.
(20) Moreira, N.; Garcia, A.; Rosa, A.; Frauenheim, T. In *SPIE Proceedings* 2012, 8263; pp 826312−826314.
(21) Jagadamma, L. K.; Abdelsamie, M.; El Labban, A.; Aresu, E.; Ndjawa, G. O. N.; Anjum, D. H.; Cha, D.; Beaujuge, P. M.; Amassian, A. *J. Mater. Chem. A* **2014**, *2*, 13321−13331.
(22) Anderson, N. C.; Hendricks, M. P.; Choi, J. J.; Owen, J. S. *J. Am. Chem. Soc.* **2013**, *135*, 18536−18548.
(23) Anderson, N. C.; Owen, J. S. *Chem. Mater.* **2013**, *25*, 69−76.
(24) Lange, I.; Reiter, S.; Pätzel, M.; Zykov, A.; Nefedov, A.; Hildebrandt, J.; Hecht, S.; Kowarik, S.; Wöll, C.; Heimel, G.; et al. *Adv. Funct. Mater.* **2014**, *24*, 7014−7024.
(25) Gliboff, M.; Li, H.; Knesting, K. M.; Giordano, A. J.; Nordlund, D.; Seidler, G. T.; Brédas, J.-L.; Marder, S. R.; Ginger, D. S. *J. Phys. Chem. C* **2013**, *117*, 15139−15147.
(26) Moreira, N. H.; Domınguez, A.; Frauenheim, T.; da Rosa, A. L. *Phys. Chem. Chem. Phys.* **2012**, *14*, 15445−15451.
(27) Choi, H.; Kim, H. B.; Ko, S. J.; Kim, J. Y.; Heeger, A. J. *Adv. Mater.* **2015**, *27*, 892−896.
(28) Ip, A. H.; Kiani, K.; Kramer, I. J.; Voznyy, O.; Movahed, H. F.; Levina, L.; Adachi, M. M.; Hoogland, S.; Sargent, E. H. *ACS Nano* **2015**, *9*, 8833−8842.
(29) Braun, S.; Salaneck, W. R.; Fahlman, M. *Adv. Mater.* **2009**, *21*, 1450−1472.
(30) Burgelman, M.; Nollet, P.; Degrave, S. *Thin Solid Films* **2000**, *361*, 527−532.
(31) Burgelman, M.; Decock, K.; Khelifi, S.; Abass, A. *Thin Solid Films* **2013**, *535*, 296−301.

DOI: 10.1021/acs.nanolett.5b03677
Nano Lett. XXXX, XXX, XXX−XXX